Anisotropic, thermal, and magnetic properties of $CeAgSb_2$: Explanation via a crystalline electric field scheme

Tetsuya Takeuchi*
Low Temperature Center, Osaka University, Toyonaka, Osaka 560-0043, Japan

Arumugam Thamizhavel, Tomoyuki Okubo, Mineko Yamada, Noriko Nakamura, Takeshi Yamamoto, Yoshihiko Inada, and Kiyohiro Sugiyama
Graduate School of Science, Osaka University, Toyonaka, Osaka 560-0043, Japan

Andrei Galatanu and Etsuji Yamamoto
Advances Science Research Center, Japan Atomic Energy Research Institute, Tokai, Ibaraki 319-1195, Japan

Koichi Kindo
KYOKUGEN, Osaka University, Toyonaka, Osaka 560-8531, Japan

Takao Ebihara
Department of Physics, Faculty of Science, Shizuoka University, 836 Ohya, Shizuoka 422-8529, Japan

Yoshichika Ōnuki
Graduate School of Science, Osaka University, Toyonaka, Osaka 560-0043, Japan
and Advances Science Research Center, Japan Atomic Energy Research Institute, Tokai, Ibaraki 319-1195, Japan

(Received 6 August 2002; revised manuscript received 24 September 2002; published 6 February 2003)

We have studied the thermal and magnetic properties of a single crystal of $CeAgSb_2$, which has a small net magnetic moment of about $0.4\mu_B$ below the ordering temperature $T_{ord}=9.7$ K, by means of specific heat, thermal expansion, and magnetization measurements. The magnetic part of the specific heat shows a broad peak around 30 K, and the magnetic entropy reaches $R \ln 4$ at about 50 K. This indicates that the first excited doublet is situated at about 50 K from the ground state. In addition, the thermal expansion along the tetragonal [001] direction exhibits a clear negative peak around 25 K, which is also attributed to the magnetic excitations between crystalline electric field (CEF) states. These data, together with the anisotropic magnetic susceptibility, were analyzed on the basis of a CEF model, and splitting energies from the ground state to the first and second excited states were estimated to be 48 and 140 K, respectively. Furthermore, the anisotropy in the high-field magnetization was well explained by the present CEF model with the same parameters, where the saturation moment for $H\|$ [001] is found to be determined by the value of $g_J J_z$ of the ground state.

DOI: 10.1103/PhysRevB.67.064403 PACS number(s): 71.20.Eh, 65.40.Ba, 65.40.De

I. INTRODUCTION

Cerium intermetallic compounds often exhibit competition between the Ruderman-Kittel-Kasuya-Yosida (RKKY) interaction and the Kondo effect, which leads to unusual ground states. Depending on the strength of the magnetic exchange interaction J_{cf} between the conduction electron (c) and $4f$ spins, either magnetic or nonmagnetic ground states are observed at low temperatures. Wherever the RKKY interaction is dominant, the magnetic ground state is stabilized by the conduction-electron-mediated indirect exchange interaction between $4f$-electron moments. The actual magnetic structure depends on the anisotropy of the RKKY interaction and the crystalline electric field (CEF).

With increasing J_{cf}, the magnetic moments of the localized $4f$ electrons are screened by the spin polarization of the conduction electrons, resulting in spin fluctuations and a reduced magnetic moment and transition temperature. A nonmagnetic Fermi-liquid state with strong spin fluctuations is established for large J_{cf} beyond the critical value of J_c at a quantum critical point. In the vicinity of the quantum critical point, a non-Fermi-liquid character and/or unconventional superconductivity have been found, and stimulating experimental and theoretical studies are in progress to clarify the interplay between magnetism and superconductivity.

In addition to this competition, as often observed in cerium Kondo systems, the CEF plays a significant role in determining their thermodynamic and magnetic properties. The CEF analysis provides information about the f levels and the wave functions of the f electron ground state involved in the hybridization effect. The CEF analysis is a starting point for theoretical analyses which extend beyond simple phenomenology. In addition, it was proposed that the CEF potential is itself largely dependent on the hybridization between the localized f-electron states and the conduction band states which are responsible for the heavy-fermion behavior.[1]

$CeAgSb_2$ crystallizes in the tetragonal $ZrCuSi_2$-type structure ($P4/nmm$) with lattice constants $a=4.363$ Å and $c=10.699$ Å.[2,3] The characteristic feature of this crystal structure is a sequential stacking of CeSb-Ag-CeSb-Sb layers along the [001] direction, as shown in Fig. 1. The electrical resistivity shows $-\ln T$ dependence with decreasing tem-

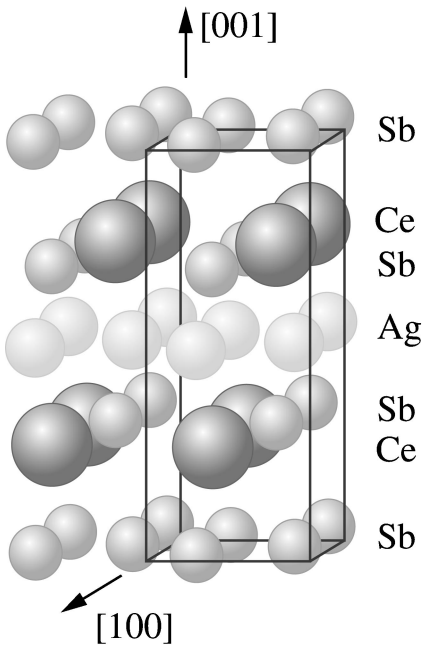

FIG. 1. Crystal structure of $CeAgSb_2$. The solid line represents the tetragonal unit cell.

perature below about 100 K and has a maximum around 20 K followed by a rapid decrease below $T_{ord}=9.7$ K.[3–5] The thermoelectric power of a polycrystalline sample[4] exhibits a maximum centered around 80 K and a plateau near 20 K. These transport properties are typical of Kondo lattice systems. In addition, preliminary inelastic neutron scattering measurements indicate a relatively high Kondo temperature T_K ($\sim$60–80 K) for this compound.[7] On the other hand, the magnetic susceptibility, magnetization, and heat capacity measurements performed on a high-quality single crystal of $CeAgSb_2$ suggest that the $4f$ electrons are localized. For instance, magnetization measurements made on a single crystal of $CeAgSb_2$ indicate ferromagnetic ordering below T_{ord}.[3] However, this magnetization shows quite anomalous behavior: the magnetization for the field along [001] indicates a typical ferromagnetic response with a saturation moment $\mu_s \sim 0.4\mu_B$, while the magnetization for [100] increases almost linearly up to 3 T and shows a saturation feature at higher fields, reaching $1.15\mu_B$ at 5 T. Furthermore, the magnetic entropy reaches almost $R\ln 2$ at T_{ord}.[3,5] The relatively large induced-moment of $1.15\mu_B$ and the entropy change below T_{ord} imply that $4f$ electrons in $CeAgSb_2$ are almost localized at low temperatures.

With regard to the magnetic structure in the ordered state, neutron powder diffraction experiments done by André *et al.* suggest that $CeAgSb_2$ is a ferromagnet below $T_c=9.5$ K with the magnetic moment of $0.33\mu_B$ aligned parallel to the [001] direction (c axis).[6] On the other hand, a simple ferrimagnetic structure[5] and a complex antiferromagnetic structure with a resultant ferromagnetic component along [001] (Refs. 3 and 4) are also proposed by bulk magnetic measurements. From the recent muon spin relaxation (μSR) measurement, Dann *et al.*[8] claim that a simple ferrimagnetic structure is not realistic, because the spectra in both the ordered and paramagnetic states indicate a single crystallographic and magnetic muon site. It is, however, extremely difficult to discriminate between a simple ferromagnetic structure and a complex antiferromagnetic structure with a ferromagnetic net moment.

The low-temperature electronic state has been studied by de Haas–van Alphen (dHvA) experiments,[9,10] and it was revealed that $CeAgSb_2$ has large cylindrical but corrugated Fermi surfaces with relatively large cyclotron masses of $(20–30)m_0$.[10] These large Fermi surfaces, which occupy about half of the Brillouin zone, are in contrast to small Fermi surfaces of $LaAgSb_2$ and $YAgSb_2$ which have a semimetallic character. These dHvA experiments indicate a quasi-two-dimensional electronic state in $CeAgSb_2$.

As stated above, both the electronic and magnetic properties in the single-crystal $CeAgSb_2$ are not explained consistently and not fully understood in spite of intensive experimental efforts. In order to get more insight into the low-temperature electronic and magnetic properties in $CeAgSb_2$, we have performed measurements of the specific heat up to 80 K, the thermal expansion up to 250 K, and in magnetic fields up to 8 T and high-field magnetization up to 50 T.

II. EXPERIMENT

Single crystals were grown by the self-flux method, as described in Ref. 3. Starting materials were 99.9% pure Ce, 99.999% pure Ag, and 99.999% pure Sb. The typical size was $8\times5\times3$ mm^3, being flat in the (001) plane. The residual resistivity ρ_0 and the residual resistivity ratio ρ_{RT}/ρ_0 were 0.19 $\mu\Omega$ cm and 430 for the current $J\parallel$ [100], indicating a high-quality sample. The specific heat was measured by the quasiadiabatic heat pulse technique in the temperature range from 0.5 to 80 K. The magnetic susceptibility and magnetization were measured by using a commercial superconducting quantum interference device (SQUID) magnetometer in the temperature range from 1.8 to 300 K and in fields up to 7 T. The measurement of thermal expansion was carried out by using a sensitive three-terminal capacitance method in the temperature range from 4.2 to 250 K. The sample was mounted in a parallel-plate capacitance cell made of oxygen-free high-conductivity copper and placed in a superconducting magnet with a maximum field of 8 T. The high-field magnetization was measured by the standard pickup coil method in fields up to 50 T, which were generated by a long-pulse magnet to avoid eddy current heating of the sample.

III. EXPERIMENTAL RESULTS

A. Specific heat

Figure 2(a) shows the temperature dependence of the specific heat in $CeAgSb_2$ and its reference sample $LaAgSb_2$. The data for $CeAgSb_2$ have a clear jump at $T_{ord}=9.7$ K, showing a distinctive phase transition, while the displayed data for $LaAgSb_2$ are used for estimation of the magnetic contribution to the specific heat of $CeAgSb_2$. Even above T_{ord}, the specific heat of $CeAgSb_2$ is obviously larger than that in $LaAgSb_2$, indicating that there is a significant mag-

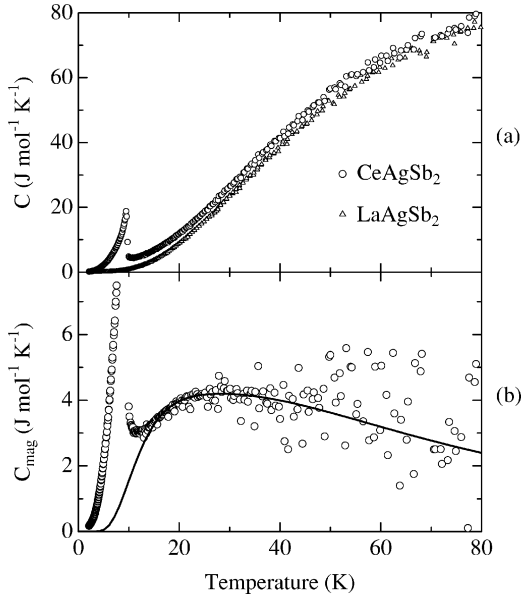

FIG. 2. Temperature dependence of the specific heat of a single crystal of $CeAgSb_2$ (circles) and $LaAgSb_2$ (triangles) (a) and magnetic specific heat C_{mag} of $CeAgSb_2$ (b). The solid line in panel (b) is a fit using the CEF model (see text).

netic contribution derived from Ce^{3+} ions above T_{ord}. The magnetic specific heat $C_{mag}=C(CeAgSb_2)-C(LaAgSb_2)$ is plotted in Fig. 2(b). A broad peak centered at about 30 K is found above T_{ord}, which is associated with the Schottky excitations arising from a CEF splitting of the Hund's-rule ground-state multiplet. The solid line is the calculated magnetic specific heat based on a CEF model, which will be discussed later.

The temperature dependence of the magnetic entropy S_{mag}, which is obtained by integrating the magnetic specific heat divided by temperature C_{mag}/T, is shown in Fig. 3. The magnetic entropy reaches almost $R\ln 2$ at T_{ord}, indicating that the ground state in the CEF scheme of the Ce^{3+} ion is a doublet. Above T_{ord}, S_{mag} gradually increases and reaches $R\ln 4$ around 50 K. In tetragonal symmetry, the degenerate sixfold levels of the ground-state multiplet of Ce^{3+} split into three doublets, and Δ_1 and Δ_2 are the excitation energies for the first and second excited states, respectively. The entropy

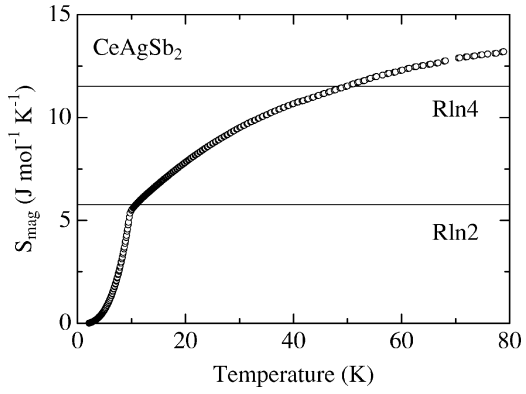

FIG. 3. Magnetic entropy S_{mag} in $CeAgSb_2$.

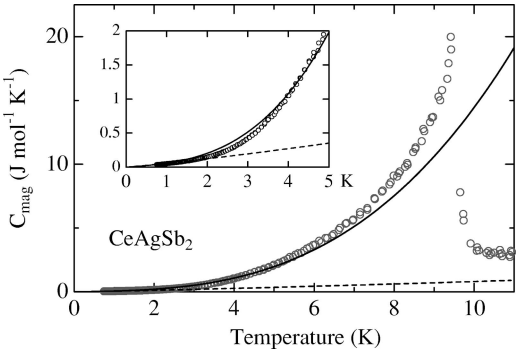

FIG. 4. Temperature dependence of the magnetic specific heat of $CeAgSb_2$. Solid and dashed lines show calculated curves on the basis of spin-wave theory for antiferromagnets and ferromagnets, respectively. The inset shows an enlarged figure at low temperatures.

change above T_{ord} suggests that the magnitude of the energy Δ_1 is about 50 K, because the entropy attains a value of $R\ln 4$ at about 50 K.

From the spin-wave theory, the temperature dependence of the magnetic specific heat for ferromagnets and antiferromagnets is proportional to $T^{3/2}$ and T^3, respectively, in a temperature range below T_{ord}. The solid line in Fig. 4 is the fitting curve with the form of $C_{mag}=\gamma T+AT^3$, where $\gamma=46\ \mathrm{mJ\,mol^{-1}\,K^{-2}}$ and $A=14\ \mathrm{mJ\,mol^{-1}\,K^{-4}}$, assuming spin-wave excitations in the antiferromagnets. The fitting is rather good below 5 K. On the other hand, the theoretical curve for ferromagnetic excitations can fit to the experimental data only below 1.5 K, as shown in Fig. 4 by a dashed line. The ferromagnetic excitation below 1.5 K is consistent with the ferromagnetic ordering below T_{ord}.[6] It is interesting that the ferromagnetic spin-wave excitation was observed only well below T_{ord}.

B. Thermal expansion

The temperature variations of the thermal expansion of $CeAgSb_2$ along [100] and [001] are shown in Fig. 5. The thermal expansion along [100] gradually decreases with lowering temperature in the whole temperature range measured, except for a weak anomaly at T_{ord} as shown in Fig. 5(b). In contrast with the above features in [100], the thermal expansion along [001] shows an unusual temperature dependence. The thermal expansion along [001] has a broad minimum around 60 K and increases for further decreasing temperature with a clear kink at T_{ord}. If the thermal expansion is composed of only the lattice contribution, it will only decrease monotonically with decreasing temperature. The negative thermal expansion for [001] indicates the presence of a substantial magnetic contribution associated with Ce^{3+} ions at low temperatures. Recently, Adroja *et al.*[11] reported similar results of the thermal expansion measurements on a single-crystal $CeAgSb_2$ and suggested that the magnetic contribution is due to the CEF effect.

The temperature dependence of the thermal expansion coefficient α, which is defined by $\alpha=d(\Delta\ell/\ell)/dT$, and the specific heat divided by temperature C/T are shown in Fig.

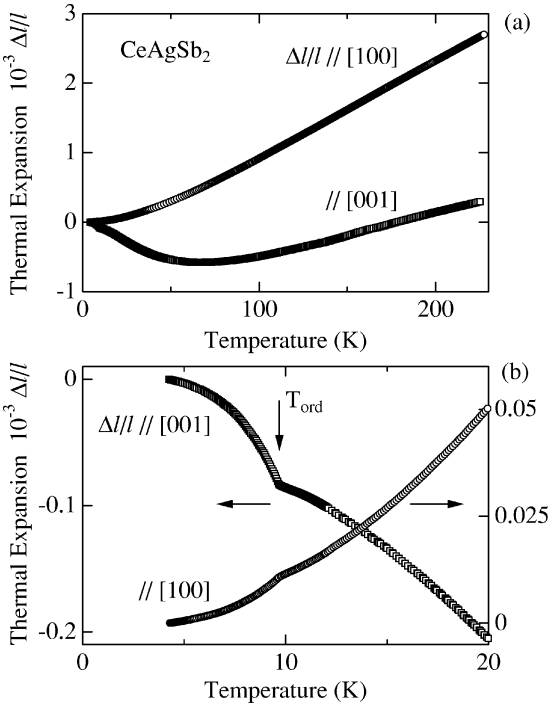

FIG. 5. Temperature dependence of the thermal expansion along [100] and [001] in $CeAgSb_2$ (a) and expanded data at low temperatures (b).

6. Clear positive and negative peaks of α were observed for [100] and [001], respectively, at the same temperature, where the specific heat exhibits the magnetic transition at $T_{\mathrm{ord}} = 9.7$ K. The initial slope of the pressure dependence of the

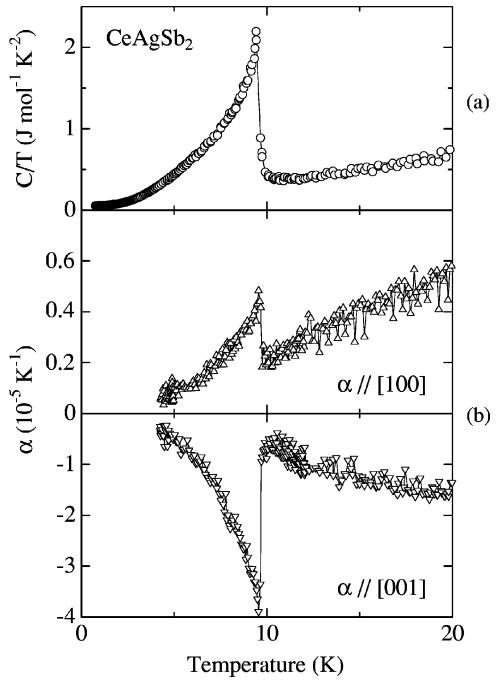

FIG. 6. Specific heat divided by temperature C/T (a) and low-temperature thermal expansion coefficient α for [100] and [001] (b) in $CeAgSb_2$.

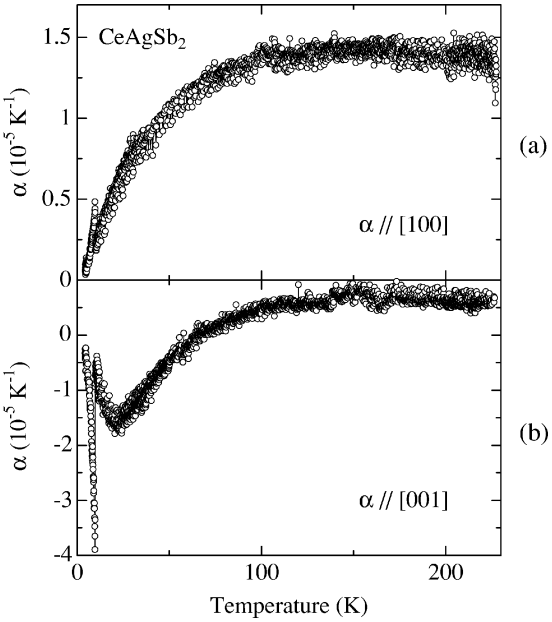

FIG. 7. Temperature dependence of the thermal expansion coefficient of $CeAgSb_2$ along (a) [100] and (b) [001].

ordering temperature can be estimated from the Ehrenfest relation by using the values of α and C/T as

$$dT_{\mathrm{ord}}/dp = \frac{V_{\mathrm{m}}\Delta\alpha_V}{\Delta(C/T)}, \tag{1}$$

where V_{m} is the molar volume, and $\Delta\alpha_V$ and $\Delta(C/T)$ are changes of the volume thermal expansion coefficient and the specific heat divided by temperature below T_{ord}. By using the experimental values of $V_{\mathrm{m}} = 1.226\times10^{-4}$ m^3/mol, $\Delta\alpha_V = -2.6\times10^{-5}$ K^{-1}, and $\Delta(C/T) = 1.65$ J mol^{-1} K^{-2}, we obtain the dT_{ord}/dp as -1.9 K/GPa. This value is comparable to the values of ~ -0.95 K/GPa (Ref. 7) and ~ -1.5 K/GPa (Ref. 12) estimated from pressure studies on the ac susceptibility and the electrical resistivity, respectively. The minus sign in dT_{ord}/dp means a suppression of T_{ord} under pressure, being consistent with hydrostatic pressure experiments.[7,12] The opposite change in α at T_{ord} suggests an opposite pressure dependence of T_{ord} when the pressure is applied uniaxitially; that is, T_{ord} will increase and decrease under uniaxial pressure along [100] and [001], respectively.

Next we show in Figs. 7(a) and 7(b) the temperature dependence of the thermal expansion coefficient α up to the maximum temperature measured for [100] and [001], respectively. At high temperatures, the thermal expansion coefficients for both directions show a Debye temperature dependence, characteristic of the phonon contribution. Below 100 K, α for [100] decreases rapidly down to 4.2 K except for the sharp peak at T_{ord}, while for [001], α shows a distinct negative dip at about 25 K, where the Schottky excitation peak was observed at about 30 K in the magnetic specific heat as shown in Fig. 2. This is in agreement with the suggestion that the negative dip in $\alpha\|$ [001] is due to the Schottky excitations between the CEF levels.

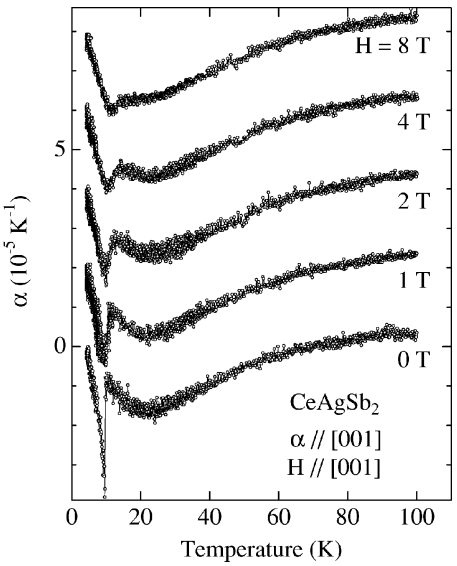

FIG. 8. Temperature dependence of the thermal expansion coefficient along [001] in magnetic fields along [001].

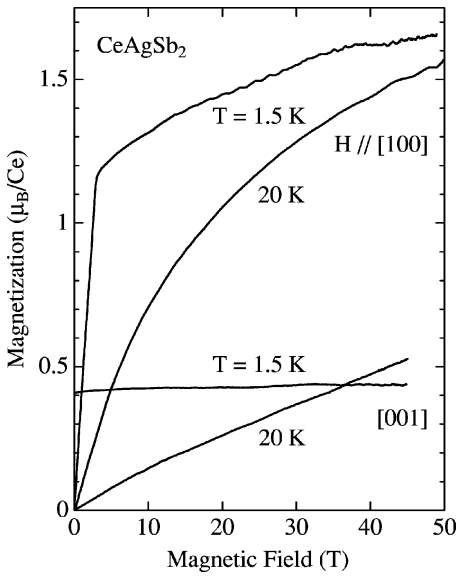

FIG. 9. High-field magnetization curves at 1.5 and 20 K for $H\|$ [100] and [001].

In order to examine the magnetic field effect, the isofield thermal expansion along [001] was measured in the field parallel to [001]. The result is plotted in Fig. 8. The peak height at T_{ord} is rapidly suppressed by applying the magnetic field, while the peak position is only slightly shifted to higher temperatures—namely, from $T_{\mathrm{ord}}(H=0)=9.7$ K to 11.5 K at 8 T. Above T_{ord}, the temperature variations of α in magnetic fields are similar to the zero-field data. It is, therefore, clear that the origin of the broad negative peak is hardly affected by a magnetic field as high as 8 T.

C. High-field magnetization and magnetic phase diagram

The magnetization of $CeAgSb_2$ below 7 T was measured by a SQUID magnetometer. The magnetization at 2 K along [001] saturates at a very low field with a saturation moment of about $0.4\mu_{\mathrm{B}}$ and remains nearly constant up to 7 T. When the field is removed, it has a remanent magnetization of $0.4\mu_{\mathrm{B}}$. On the other hand, the magnetization along [001] increases almost linearly up to about $1.2\mu_{\mathrm{B}}$ around 3 T and slowly increases at higher fields. These values are in good agreement with a previous study.[3] To understand this anomalous magnetization curve, we have measured the high-field magnetization by using a long-pulse magnet. The high-field magnetization curves for both directions at 1.5 and 20 K are shown in Fig. 9. The magnetization along [100] at 1.5 K increases linearly but suddenly changes its slope at around 3 T. For further increasing the magnetic field, the magnetic moment gradually develops up to 50 T, reaching $1.65\mu_{\mathrm{B}}$ at the maximum field. It is clear that higher fields are necessary to saturate the magnetization for $H\|$ [100]. This characteristic feature is typical of an antiferromagnetic compound. At 20 K, which is above T_{ord}, the kink in the magnetization at 1.5 K disappears, and the magnetization increases monotonically to $1.57\mu_{\mathrm{B}}$ at 50 T. The magnetization along [001] is more intriguing. The magnetization at 1.5 K remains nearly constant at high fields, showing a saturation moment of about $0.4\mu_{\mathrm{B}}$. Furthermore, the magnetization at 20 K increases almost linearly and exceeds $0.4\mu_{\mathrm{B}}$ in the field above 36 T. The reason for this crossing of the magnetization curves will be discussed later.

Figure 10 shows the differential magnetization dM/dH for $H\|$ [100] at several temperatures. A steplike anomaly in the dM/dH curves corresponds to a slope change in the magnetization as seen in Fig. 9. This anomaly shifts to lower fields with raising the temperature and disappears at 10.1 K which is just above T_{ord}. The transition fields are determined at the midpoint of the anomaly as shown by arrows and plotted in the H-T space as shown in Fig. 11 by open circles. Open squares represent the magnetic field values where the magnetization isotherm along [100], measured by a SQUID

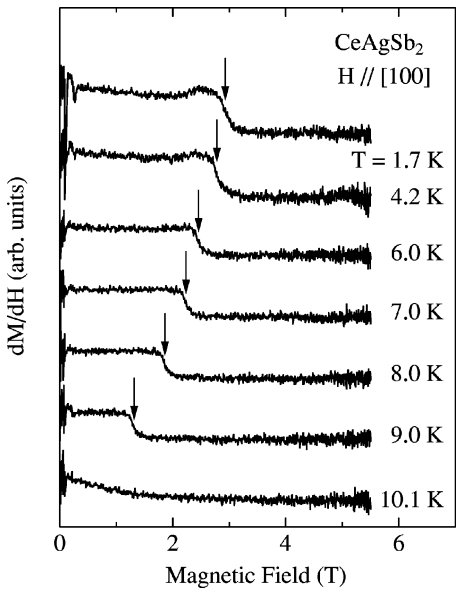

FIG. 10. Differential magnetization curves for the field along [100] in $CeAgSb_2$ at selected temperatures.

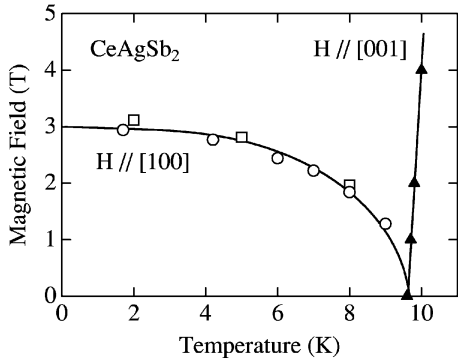

FIG. 11. Magnetic phase diagram in $CeAgSb_2$. Open circles and squares are the transition fields for $H\|$ [100] determined from pulsed field (Fig. 10) and SQUID magnetization measurements, respectively. Solid triangles represent the transition temperatures for $H\|$ [001] determined from the isofield thermal expansion data shown in Fig. 8.

magnetometer, changes its slope. These transition points can be traced by one line which is connected smoothly to $T_{ord} = 9.7$ K at zero magnetic field. This means that these transitions in the magnetization along [100] are related to the magnetic ordering at T_{ord}.

In contrast to $H\|$ [100], the transition temperature slightly shifts to a higher temperature when we apply a magnetic field along [001] as shown by solid triangles. This behavior of the transition temperature in the magnetic field seems to be consistent with the ferromagnetic transition at T_{ord}.[3,6] It is, however, not clear why the magnetization curve as well as the magnetic phase diagram shows different characteristics depending on the crystallographic axis.

IV. ANALYSES AND DISCUSSION

A. Estimation of the lattice contribution to the thermal expansion

In order to analyze the thermal expansion coefficient, we should know the temperature dependence of the lattice contribution which is expressed by the Debye function. According to the Grüneisen relation, the thermal expansion coefficient is related to the specific heat as

$$\alpha = \frac{\Gamma C_V}{B_T V}, \tag{2}$$

where Γ is the Grüneisen parameter, B_T the bulk modulus, and C_V the specific heat at constant volume. This equation means that the temperature dependence of the thermal expansion is approximately the same as that of the specific heat. On the basis of the Debye model, the lattice specific heat is given by

$$C_V = 9Nk_B\left(\frac{T}{\Theta_D}\right)^3 \int_0^{\Theta_D/T} \frac{x^4 e^x}{(e^x-1)^2} dx, \tag{3}$$

where N is the number of atoms, k_B the Boltzmann constant, and Θ_D the Debye temperature.

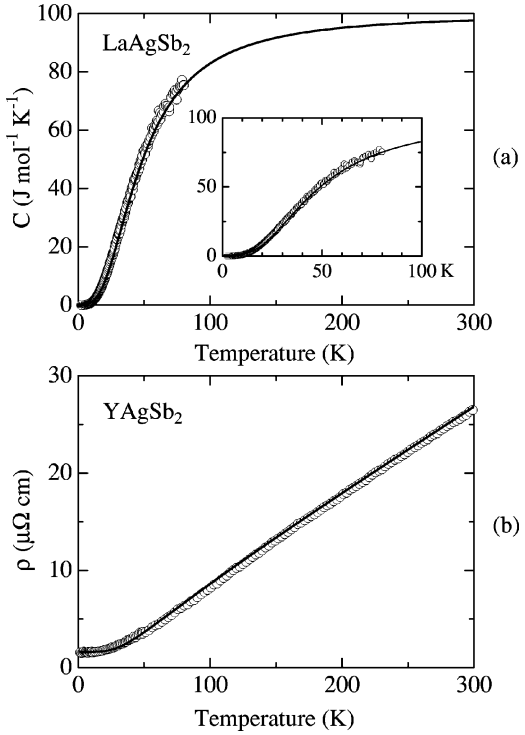

FIG. 12. Temperature dependence of (a) the specific heat in $LaAgSb_2$ and (b) electrical resistivity in $YAgSb_2$ (after Ref. 3). Solid lines show the theoretical curves based on the Debye model with $\Theta_D = 196$ K.

In order to estimate the value of Θ_D, we fitted Eq. (3) to the specific heat data of $LaAgSb_2$ as shown in Fig. 12(a). Over all specific heat data of $LaAgSb_2$ is well expressed by Eq. (3), and the Debye temperature is thus estimated to be 196 K. By using the same Debye temperature, we calculated the temperature dependence of the resistivity by using the expression

$$\rho(T) = \rho_0 + AT^5 \int_0^{\Theta_D/T} \frac{x^5}{(e^x-1)(1-e^{-x})} dx, \tag{4}$$

where ρ_0 is the residual resistivity, A is a numerical constant, and the second term is due to the phonon-assisted electron scattering. As shown in Fig. 12(b), $\rho(T)$ for $YAgSb_2$ (Ref. 3) is well described by Eq. (4) with $\Theta_D = 196$ K. We have used this value as the Debye temperature for the lattice contribution to the thermal expansion, although this value is slightly smaller than the previously reported values of $\Theta_D = 249$ K (Ref. 5) and 220 K (Ref. 10) estimated from the low-temperature specific heat data.

B. Crystalline electric field analysis

The specific heat and thermal expansion coefficient show broad peaks with a long tail towards higher temperatures as shown in Figs. 2 and 7. These features are probably due to the Schottky excitations between the CEF levels of Ce^{3+}

ions. We analyze these data, together with the magnetic susceptibility, on the basis of the CEF model as follows. The CEF Hamiltonian for tetragonal symmetry can be expressed as

$$\mathcal{H}_{\mathrm{CEF}}=B_2^0O_2^0+B_4^0O_4^0+B_4^4O_4^4, \tag{5}$$

where B_ℓ^m and O_ℓ^m are the CEF parameters and the Stevens operators, respectively.[13,14] Due to the CEF effect, the sixfold-degenerated $4f$ levels are split into three doublets with excitation energies Δ_1 and Δ_2 from the ground to the first and second excited states, respectively. In this case, the Schottky specific heat can be written as

$$C_{\mathrm{sch}}=\left(\frac{R}{(k_{\mathrm{B}}T)^2}\right)\frac{e^{(\Delta_1+\Delta_2)/k_{\mathrm{B}}T}\{-2\Delta_1\Delta_2+\Delta_2^2(1+e^{\Delta_1/k_{\mathrm{B}}T})+\Delta_1^2(1+e^{\Delta_2/k_{\mathrm{B}}T})\}}{(e^{\Delta_1/k_{\mathrm{B}}T}+e^{\Delta_2/k_{\mathrm{B}}T}+e^{(\Delta_1+\Delta_2)/k_{\mathrm{B}}T})^2}. \tag{6}$$

The magnetic contribution to the thermal expansion coefficient can be estimated from the following equation[15]:

$$\begin{aligned}\alpha_{\mathrm{CEF}}^i&=B_i\left(\frac{1}{k_{\mathrm{B}}T^2}\right)(\langle O_2^0E\rangle-\langle O_2^0\rangle\langle E\rangle)\\&=B_i\left(\frac{1}{k_{\mathrm{B}}T^2}\right)\left(\frac{\sum_n \mu_nE_ne^{-E_n/k_{\mathrm{B}}T}}{Z}\right.\\&\quad\left.-\frac{\sum_n \mu_ne^{-E_n/k_{\mathrm{B}}T}}{Z}\frac{\sum_n E_ne^{-E_n/k_{\mathrm{B}}T}}{Z}\right),\end{aligned} \tag{7}$$

where μ_n is defined by $\langle n|O_2^0|n\rangle$, E_n and $|n\rangle$ are the nth eigenvalue and eigenfunction, respectively, and $Z=\Sigma_n e^{-E_n/k_{\mathrm{B}}T}$. B_i ($i=[100]$ and $[001]$) is a fitting parameter for the principal axis. The total thermal expansion coefficient above the ordering temperature is expressed by the sum of the lattice and magnetic parts as

$$\alpha_{\mathrm{total}}^i=\alpha_{\mathrm{lattice}}^i+\alpha_{\mathrm{CEF}}^i \quad (i=[100]\ \text{and}\ [001]). \tag{8}$$

The lattice contribution $\alpha_{\mathrm{lattice}}^i$ is calculated on the basis of Eqs. (2) and (3) with $\Theta_{\mathrm{D}}=196$ K, where $(\Gamma/B_{\mathrm{T}}V)$ in Eq. (2) is assumed to be constant and treated as an adjustable parameter for each axis. The CEF contribution α_{CEF}^i is calculated on the basis of the Grüneisen relation [Eq. (2)] by using C_{sch}. This result is same as that obtained from Eq. (7).

The CEF susceptibility is given by

$$\begin{aligned}\chi_{\mathrm{CEF}}^i&=N(g_J\mu_{\mathrm{B}})^2\frac{1}{Z}\left(\sum_{m\neq n}|\langle m|J_i|n\rangle|^2\right.\\&\quad\times\frac{1-e^{-\Delta_{m,n}/k_{\mathrm{B}}T}}{\Delta_{m,n}}e^{-E_n/k_{\mathrm{B}}T}\\&\quad\left.+\frac{1}{k_{\mathrm{B}}T}\sum_n|\langle n|J_i|n\rangle|^2e^{-E_n/k_{\mathrm{B}}T}\right),\end{aligned} \tag{9}$$

where g_J is the Landé g factor (6/7 for Ce^{3+}), J_i ($i=x$, y and z) is the component of the angular momentum, and $\Delta_{m,n}=E_n-E_m$. The magnetic susceptibility including the molecular field contribution is given as follows:

$$\chi_i^{-1}=(\chi_{\mathrm{CEF}}^i)^{-1}-\lambda_i. \tag{10}$$

The CEF parameters were determined so as to reproduce the specific heat and thermal expansion as well as susceptibility data, which are in agreement with the preliminary results of inelastic neutron scattering experiments.[17] The solid lines in Figs. 2, 13, and 14 show the calculated curves by using the CEF parameters listed in Table I. The magnetic specific heat above T_{ord} is well explained by the CEF model as shown in Fig. 2. Furthermore, the estimated energy splitting $\Delta_1=48$ K is consistent with the entropy change shown in Fig. 3, since the magnetic entropy reaches $R\ln 4$ around 50 K.

As regards to the temperature dependence of the thermal expansion coefficient, characteristic features can be ex-

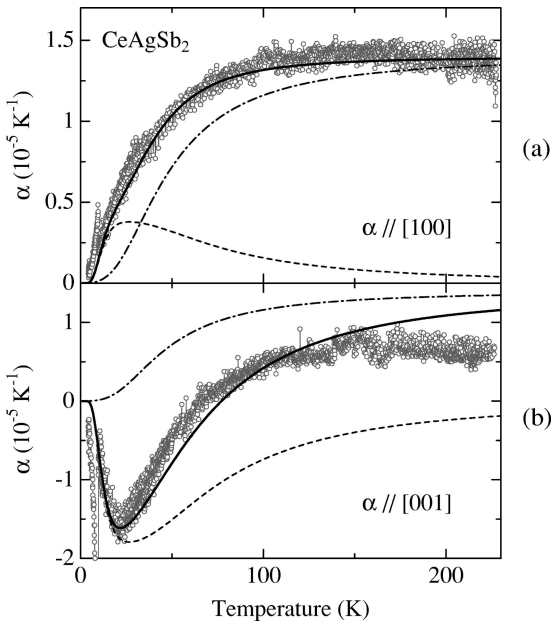

FIG. 13. Temperature dependence of the thermal expansion coefficient of $CeAgSb_2$ along (a) [100] and (b) [001]. Dashed and dash-dotted lines show the magnetic (α_{CEF}) and the lattice ($\alpha_{\mathrm{lattice}}$) contributions, respectively. Solid lines are the sum of $\alpha_{\mathrm{lattice}}$ and α_{CEF}. Fitting parameters are $(\Gamma/B_{\mathrm{T}}V)_{[100]}=1.4\times10^{-7}$ mol/J and $B_{[100]}=5.7\times10^{-5}$ for [100] and $(\Gamma/B_{\mathrm{T}}V)_{[001]}=1.4\times10^{-7}$ mol/J and $B_{[001]}=-2.8\times10^{-4}$ for [001].

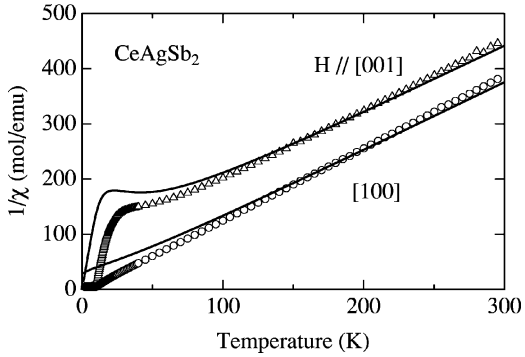

FIG. 14. Temperature dependence of the inverse magnetic susceptibility in $CeAgSb_2$. Solid lines are the calculated curves based on the CEF model.

plained by the calculated curves as shown in Fig. 13, although there is a small deviation at high temperatures for [001]. This may be due to the simple estimation of the lattice contribution at high temperatures. The temperature dependence of the thermal expansion coefficient under magnetic fields are also calculated by using the same parameters, and it is found that they are hardly changed by magnetic fields up to 8 T. This is also consistent with the experimental results as shown in Fig. 8. It is interesting to note that the magnetic contribution to the thermal expansion coefficient has positive and negative peaks for [100] and [001] directions, respectively. Such an opposite magnetic contribution has also been observed in tetragonal $CeRhIn_5$.[16] One of the common characteristics between $CeAgSb_2$ and $CeRhIn_5$ is the quasi-two-dimensionality in their electronic states.[9] This may be the reason for the opposite magnetic contribution in the thermal expansion coefficient.

As shown in Fig. 14, calculated susceptibility curves approximately agree with the experimental results, although there are small differences above 100 K. The magnetic susceptibility in $CeAgSb_2$ follows the Curie-Weiss law in the temperature range above 100 K, but the estimated effective moments are somewhat smaller than the theoretical value of $2.54\mu_B$/Ce for Ce^{3+}: namely, $2.47\mu_B$/Ce for [100] and $2.48\mu_B$/Ce for [001]. This is why the slope of the experimental inverse susceptibility curve above 100 K becomes larger than that of the theoretical one.

It is noted that CEF excitations in $CeAgSb_2$ were observed by recent inelastic neutron scattering experiments.[11,17] The present CEF level scheme is consistent with the observed excitation energies of 5.1 meV ($\sim$59 K) and 12.4 meV ($\sim$144 K). Furthermore, the small mixing between $|\pm 3/2\rangle$ and $|\pm 5/2\rangle$ states is also consistent with the fact that the observed excitation intensity at 12.4 meV is very weak compared to that at 1.5 meV.[17] From this analysis, it is found that the CEF ground state in $CeAgSb_2$ is $|\pm 1/2\rangle$, and the first and second excited levels are dominated by $|\pm 3/2\rangle$ and $|\pm 5/2\rangle$ states, respectively.

C. Magnetization based on the CEF model

Next we discuss the magnetization on the basis of the CEF model. The magnetization can be calculated by

$$M_i = g_J \mu_B \sum_n |\langle n|J_i|n\rangle| \frac{e^{-E_n/k_B T}}{Z} \quad (i = x,\ y,\ \text{and}\ z). \tag{11}$$

The eigenvalue E_n and the eigenfunction $|n\rangle$ are determined by diagonalizing the total Hamiltonian

$$\mathcal{H} = \mathcal{H}_{CEF} - g_J \mu_B J_i (H_i + \lambda_i M_i), \tag{12}$$

where $\mathcal{H}_{CEF}$ is given by Eq. (5), the second term is the Zeeman term, and the third one is from the molecular field. In Fig. 15, we show the calculated magnetization curves by using the same CEF parameters as in Table I and replot the experimental curves by thick solid lines which were already shown in Fig. 9. For $H \parallel$ [100], the calculated magnetization shows a gradual increase up to about 100 T and almost saturates at higher fields. On the other hand, the calculated magnetization for $H \parallel$ [001] at 1.5 K indicates three steps as shown in Fig. 15(b). These step magnetizations are due to the level crossing in the CEF scheme. The magnetic field dependence of CEF energy levels for $H \parallel$ [100] and [001] is shown in Figs. 16(a) and 16(b), respectively. When the magnetic field is applied along [001], degenerate levels are split and

TABLE I. CEF parameters, energy level schemes, and corresponding wave functions for $CeAgSb_2$.

CEF parameters						
	B_2^0 (K)	B_4^0 (K)	B_4^4 (K)	λ_i (emu/mol)$^{-1}$		
	7.55	-0.02	-0.64	$\lambda_{[100]} = -28$		
				$\lambda_{[001]} = 0$		
Energy levels and wave functions						
E (K)	$\|+5/2\rangle$	$\|+3/2\rangle$	$\|+1/2\rangle$	$\|-1/2\rangle$	$\|-3/2\rangle$	$\|-5/2\rangle$
140	0.982	0	0	0	-0.189	0
140	0	0.189	0	0	0	-0.982
48	0	-0.982	0	0	0	-0.189
48	0.189	0	0	0	0.982	0
0	0	0	1	0	0	0
0	0	0	0	1	0	0

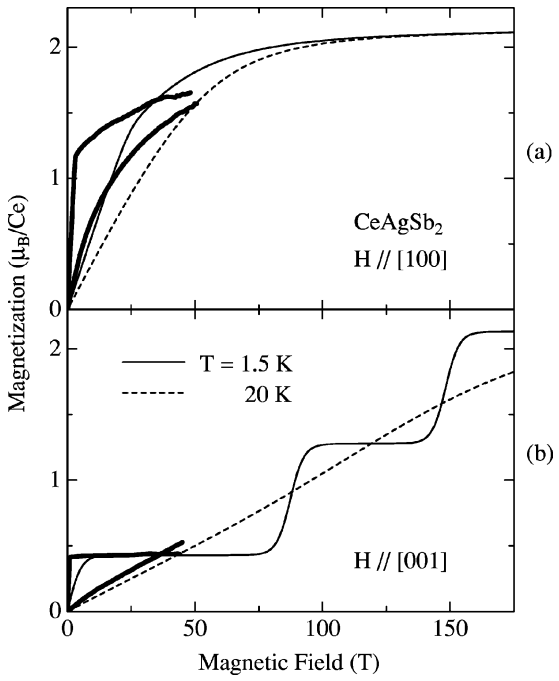

FIG. 15. Magnetization curves for the field along (a) [100] and (b) [001] in $CeAgSb_2$. Solid and dashed lines are the calculated curves based on the CEF model for 1.5 and 20 K, respectively. Thick solid lines represent the experimental magnetization at 1.5 and 20 K.

the energy of each state changes almost linearly with increasing magnetic field except for a crossover around 40 T between the first and second excited states. The metamagnetic transitions at 87 and 148 T in Fig. 15(b) are due to the $4f$-level crossing in the ground state, where the wave function changes from a $|-1/2\rangle$- to $|-3/2\rangle$-dominated state and from a $|-3/2\rangle$- to $|-5/2\rangle$-dominated state, respectively, as shown by two arrows in Fig. 16(b). Since the energy of the ground state decreases linearly with increasing field except the slope change at transition fields, the magnetization stays constant below and above the transition fields. The value of the magnetization plateau corresponds to the $g_J J_z$ value for the each state: that is, 0.43, 1.29, and 2.14 for the first, second, and third steps, respectively. At 20 K, the magnetization increases almost linearly, crossing the midpoint of the magnetization plateau at 1.5 K.

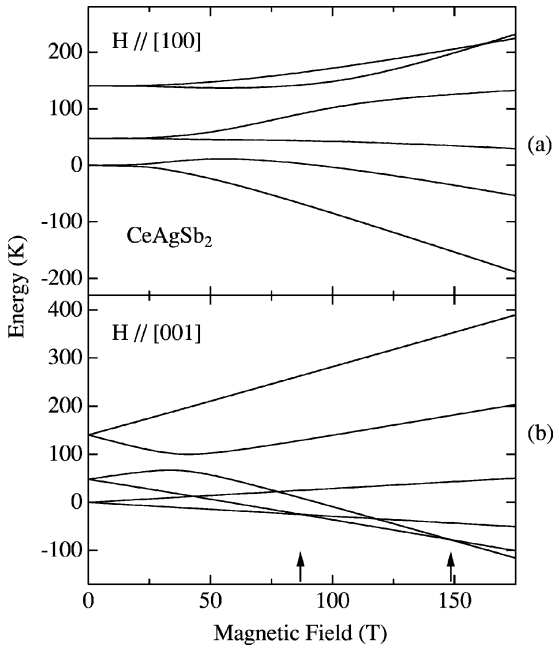

FIG. 16. Magnetic field dependence of CEF energy levels for the field along (a) [100] and (b) [001] in $CeAgSb_2$.

From the comparison between the calculated and experimental curves, it is concluded that the observed anisotropy in the magnetization curve is determined by the CEF effect. In particular, the observed crossing behavior of the magnetization for $H\|$ [001] around 40 T is well explained by the calculated magnetization. Furthermore, it should be noted that the value of the saturation moment at 1.5 K for $H\|$ [001] agrees very well with the calculated value, although it is in the ordered state. This indicates that the saturation moment of about $0.4\mu_B$ is defined by the $g_J J_z$ value of the ground state.

As for the ground-state magnetic structure, neutron scattering experiments suggest that the magnetic moments are oriented ferromagnetically along [001] with the value of $0.3\mu_B$–$0.75\mu_B$.[6,8] On the other hand, complicated structures such as a ferrimagnetic and a canted state have also been suggested by bulk measurements.[3–5] The observed magnetization along [001] at 1.5 K saturates at very low field and remains almost constant up to 45 T, showing about $0.4\mu_B$. It seems, therefore, difficult to consider the complicated structures for the ordered state. The rather small ordered moment in $CeAgSb_2$ may also be due to the CEF effect. Nevertheless, it is still not clear why the ordered magnetic moments are aligned along the [001] direction and the magnetization for $H\|$ [100] shows antiferromagnetic features. Precise neutron scattering experiments are necessary to understand the ground-state magnetic structure as well as the real nature of the spin-wave excitation, and these are in progress.

V. CONCLUSION

We have studied the electronic and magnetic properties of a single crystal of $CeAgSb_2$ by measuring the specific heat, thermal expansion, and high-field magnetization. In the paramagnetic phase, the specific heat and thermal expansion show a broad peak with a long tail towards higher temperatures around 30 K and 25 K, respectively. These data as well as the susceptibility are analyzed on the basis of the CEF model with splitting energies $\Delta_1 = 48$ K and $\Delta_2 = 140$ K from the ground state to first and second excited states, respectively. In the ordered state, the high-field magnetization along [100] shows a kink around 3 T and gradually increases up to 50 T, reaching $1.65\mu_B$. On the other hand, the magnetization along [001] saturates at about $0.4\mu_B$ and remains almost constant in high fields up to 45 T. This saturation moment is in good agreement with the value of $g_J J_z = 0.43$ for $|\pm 1/2\rangle$ of the ground state in the CEF scheme. In addition, the anisotropy of the magnetization is also well explained by the CEF model with the same parameters.

ACKNOWLEDGMENTS

We are very grateful to Dr. S. Araki and Dr. N. Metoki for helpful discussions on the crystal structure and CEF excitations in neutron scattering experiments. We would like to thank also Professor S. Ramakrishnan for a critical reading of the manuscript. This work was supported by a Grant-in-Aid for Scientific Research COE Research (No. 10CE2004) from the Ministry of Education, Culture, Sports, Science and Technology.

*Also at KYOKUGEN, Osaka University, Toyonaka, Osaka 560-8531, Japan. Electronic address: takeuchi@rcem.osaka-u.ac.jp

[1] P.M. Levy and S. Zhang, Phys. Rev. Lett. **62**, 78 (1989).
[2] M. Brylak, M.H. Möller, W. Jeitschko, P. Rogl, and O. Bodak, J. Solid State Chem. **115**, 305 (1995).
[3] K.D. Myers, S.L. Bud'ko, I.R. Fisher, Z. Islam, H. Kleinke, A.H. Lacerda, and P.C. Canfield, J. Magn. Magn. Mater. **205**, 27 (1999).
[4] M. Houshiar, D.T. Adroja, and B.D. Rainford, J. Magn. Magn. Mater. **140-144**, 1231 (1995).
[5] Y. Muro, N. Takeda, and M. Ishikawa, J. Alloys Compd. **257**, 23 (1997).
[6] G. André, F. Bourée, M. Kolenda, B. Leśniewska, A. Oleś, and A. Szytua, Physica B **292**, 176 (2000).
[7] M.J. Thornton, J.G.M. Armitage, G.J. Tomka, P.C. Riedi, R.H. Mitchell, M. Houshiar, D.T. Adroja, B.D. Rainford, and D. Fort, J. Phys.: Condens. Matter **10**, 9485 (1998).
[8] J.A. Dann, A.D. Hillier, J.G.M. Armitage, and R. Cywinski, Physica B **289-290**, 38 (2000).
[9] K.D. Myers, S.L. Bud'ko, V.P. Antropov, B.N. Harmon, P.C. Canfield, and A.H. Lacerda, Phys. Rev. B **60**, 13 371 (1999).
[10] Y. Inada, A. Thamizhavel, H. Yamagami, T. Takeuchi, Y. Sawai, S. Ikeda, H. Shishido, T. Okubo, M. Yamada, K. Sugiyama, N. Nakamura, T. Yamamoto, K. Kindo, T. Ebihara, A. Galatanu, E. Yamamoto, R. Settai, and Y. Onuki (unpublished).
[11] D.T. Adroja, P.C. Riedi, J.G.M. Armitage, and D. Fort, cond-mat/0206505 (unpublished).
[12] M. Nakashima *et al.*, J. Phys.: Condens. Matter (to be published).
[13] K.W.H. Stevens, Proc. Phys. Soc., London, Sect. A **65**, 209 (1952).
[14] M. T. Hutchings, in *Solid State Physics: Advances in Research and Applications*, edited by F. Seitz and B. Turnbull (Academic, New York, 1965), Vol. 16, p. 227.
[15] P. Morin, J. Rouchy, and D. Schmitt, Phys. Rev. B **37**, 5401 (1988).
[16] T. Takeuchi, T. Inoue, K. Sugiyama, D. Aoki, Y. Tokiwa, Y. Haga, K. Kindo, and Y. Onuki, J. Phys. Soc. Jpn. **70**, 877 (2001).
[17] S. Araki and N. Metoki (private communication).